Seismic resolution enhancement in shale-oil reservoirs

Xiwu Liu [1], Fengxia Gao [2, *], Yuanyin Zhang [3], Ying Rao [4], Yanghua Wang [5]

1. State Energy Center for Shale Oil Research and Development, Sinopec Key Laboratory of Shale Oil and Gas Exploration and Production, Sinopec Petroleum Exploration and Production Research Institute, Beijing 100081, China. E-mail: liuxw.syky@sinopec.com.

2. School of Geophysics and Information Technology, China University of Geosciences (Beijing), Beijing 100081, China. E-mail: fengxia.gao@cugb.edu.cn.

3. Oil and Gas Survey, China Geological Survey, Beijing 100029, China. E-mail: yuanyinshou@163.com.

4. State Key Laboratory of Petroleum Resources and Prospecting, China University of Petroleum (Beijing), Beijing 102249, China, and Centre for Reservoir Geophysics, Department of Earth Science and Engineering, Imperial College London, London SW7 2BP, UK. E-mail: raoying@cup.edu.cn.

5. Centre for Reservoir Geophysics, Department of Earth Science and Engineering, Imperial College London, London SW7 2BP, UK. E-mail: yanghua.wang@imperial.ac.uk.

* Corresponding author.

ABSTRACT

We developed a case study of seismic resolution enhancement for shale-oil reservoirs in the Q Depression, China, featured by rhythmic bedding. We proposed an innovative methodology for the resolution enhancement, a full-band extension method, and implemented this method in three consecutive steps: wavelet extraction, filter construction and data filtering. First, we extracted a constant-phase wavelet from the entire seismic data set. Then, we constructed the full-band extension filter in the frequency domain using the least-squares inversion method. Finally, we applied the band extension filter to the entire seismic data set. We demonstrated that this full-band extension method, with a stretched frequency band from 7-70 Hz to 2-90 Hz, may significantly enhance the 3D seismic resolution and distinguish reflection events of the rhythmite groups in shale-oil reservoirs.

INTRODUCTION

In this paper, we present a case study of enhancing seismic resolution for shale-oil reservoirs. We have a 3D seismic data set which was acquired from the Q Depression, centered at Jianghan salt-lake basin, China. Our objective of the study is to enhance the seismic resolution to characterize the feature of rhythmic bedding that shows a clear repetition of zones of formation and composition. The rhythmite groups are the potential target of shale-oil reservoirs.

The shale-oil reservoir is an unconventional oil reservoir in which the oil is produced from shale rock fragments by pyrolysis, hydrogenation, or thermal dissolution, usually stored in the pores of dark shale, fractures and the interlayers of sandstone and carbonate rocks. Shale-oil reservoirs are commonly distributed in fault basins, and the Q Depression in Jianghan salt-lake basin is one such fault basin, featured by salt rhythmic bedding. These salt rhythmite groups were developed because of the special depositional environment. During deposition, salt beds belonging to the Q group were formed. Because of the influences from a single continental source, a high salinity, strong

evaporation climate and drought climate alternation during the deposition, the lithofacies of the salt beds in the Q Depression (Figure 1), from northwest to southeast, were sand-shale facies, shale facies, clastic-evaporites (salt) facies, corresponding to depositions of freshwater zone, fresh-salt water transmission zone, and salt rhythmite zone, respectively (Huang *et al*., 2002; Zheng, 2010; Hou *et al*., 2017). The study area is located in the salt rhythmite zone. The stratigraphic sequence is listed in Figure 2.

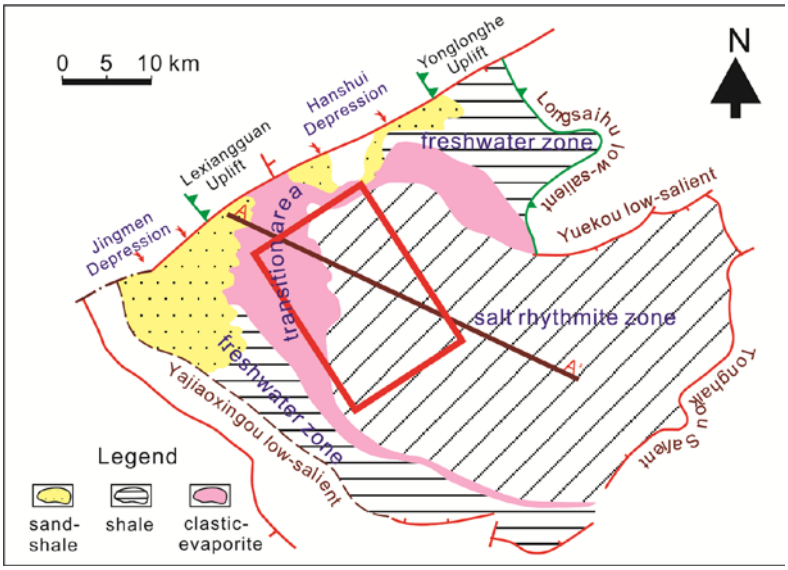

Figure 1. The lithology-lithofacies in the Q Depression, Jianghan salt lake basin, China. The red rectangular area is covered by the 3D seismic data set of this paper.

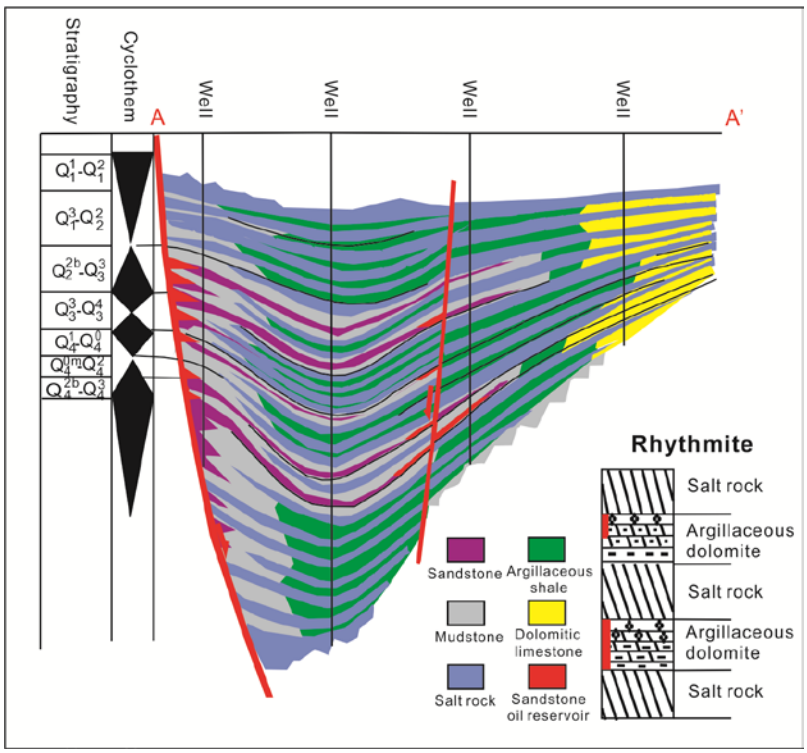

Figure 2. Sequential stratigraphy and reservoir distribution of the Q Depression. The profile is along the dark red line A-A' in Figure 1. The first column is the stratigraphy, where Q_j^k indicates the lithofacies of the *j*th formation and the *k*th subgroup in the Q Depression. The second column illustrates the sedimentary cycle. The right bottom corner is a sketch map of salt rhythmite groups.

The thickest layer within a rhythmite in the Q Depression is about 38 m, and the average thickness is between 5 and 20 m in general (Feng, 2002). The dominant frequency of the raw seismic data is about 25 Hz. After data processing, the dominant frequency is increased to about 41 Hz. The local average P-wave velocity is 3500 m/s, and thus the pre-processing has changed the dominant wavelength from 140 m to 85 m. However, the thickness of the layers is relatively thin compared to the seismic wavelength. We attempt to further improve the vertical resolution of the seismic data, so that we are able to identify the rhythmite groups.

Resolution enhancement methods include prediction deconvolution (Robinson, 1967; Robinson and Treitel, 1967; Peacock and Treitel, 1969), Gabor deconvolution (Margrave *et al*., 2005, 2011; Chen *et al*., 2013), and inverse-*Q* filtering (Wang, 2002; Guo and Wang, 2004; Zhao and Wang, 2004; Wang, 2006, 2008; Gan *et al*., 2009) and so on. However, we have a fine processed seismic data set with a relative high dominant frequency (41 Hz against 25 Hz). The data set has been processed by either inverse *Q*-filtering or predictive deconvolution. We need to derive another step to further improve the resolution.

In this study we apply a full-band extension method, to enhance the seismic resolution in shale-oil reservoirs. This method increases the dominant frequency and extends the bandwidth of the seismic data. Band extension is frequency dependent as it extends the band in both the high and low frequency parts. The extension of low frequencies will suppress the side-slobs of wavelets and make the reflection events distinguishable. This is a significant feature different from commonly used resolution enhancement methods.

GEOLOGICAL SETTING AND SEISMIC DATA

Figure 2 shows a profile of the stratigraphic sequence patterns and the reservoir distribution of the Q Depression. The profile is along the dark red line drawn in Figure 1. In Figure 2, the lithology-lithofacies of Q_j^k in the first column indicates the *j*th formation and the *k*th subgroup in the Q Depression. The additional superscripts of either ‘m’ or ‘b’ indicate the middle and bottom part of the formation, respectively. Figure 1 displays the lithology-lithofacies of Q_3^4 formation in the Q Depression. The second column indicates the sedimentary cycle.

In this study area, argillaceous shale and dolomitic limestone are interbedded with salt rocks, which compose of a salt rhythmite. The structure map can be simplified as that shown at the right bottom corner of Figure 2. Shale in this pattern is not only the source rock but also the reservoir for shale-oil resources (Fang, 2002). Therefore, the identification of rhythmites is of importance for shale-oil exploration and production.

We have a 3D seismic cube that covers 337.5 km^2 on the surface and consists of 599 inlines and 1801 crosslines. The inline numbers are 701-1299 and the crossline numbers are 500-2300 (Figure 3a). The inlines and crosslines are regularly spaced with line interval of 25 m and 12.5 m, respectively. The time sampling rate is 2 ms, and the total time length of a seismic trace is 3 s.

This 3D seismic data cube has been pre-processed, including predictive deconvolution and inverse *Q* filtering for the attenuation compensation (Wang, 2002). Because the high-frequency components of the 3D seismic data have been compensated, an inline profile displayed in Figure 3b shows a high resolution, when compared to conventional seismic profiles. However, in this study we attempt to further improve the resolution, as shown in Figure 3c, in order to clearly identify the salt rhythmites.

To further improve the resolution in this paper, we present a full-band extension method. This method will further compensate for the amplitudes of high-frequency components and shift the dominant frequency to a higher frequency. Equally important, this method will strengthen also the amplitudes of low-frequency components. Seismic resolution depends not only upon the dominant frequency but also upon the bandwidth (Zhou *et al*., 2007). Especially, when extending the

low-frequencies, the side-slobs of wavelets will be suppressed effectively, so that the reflection events of thin layers can be identified.

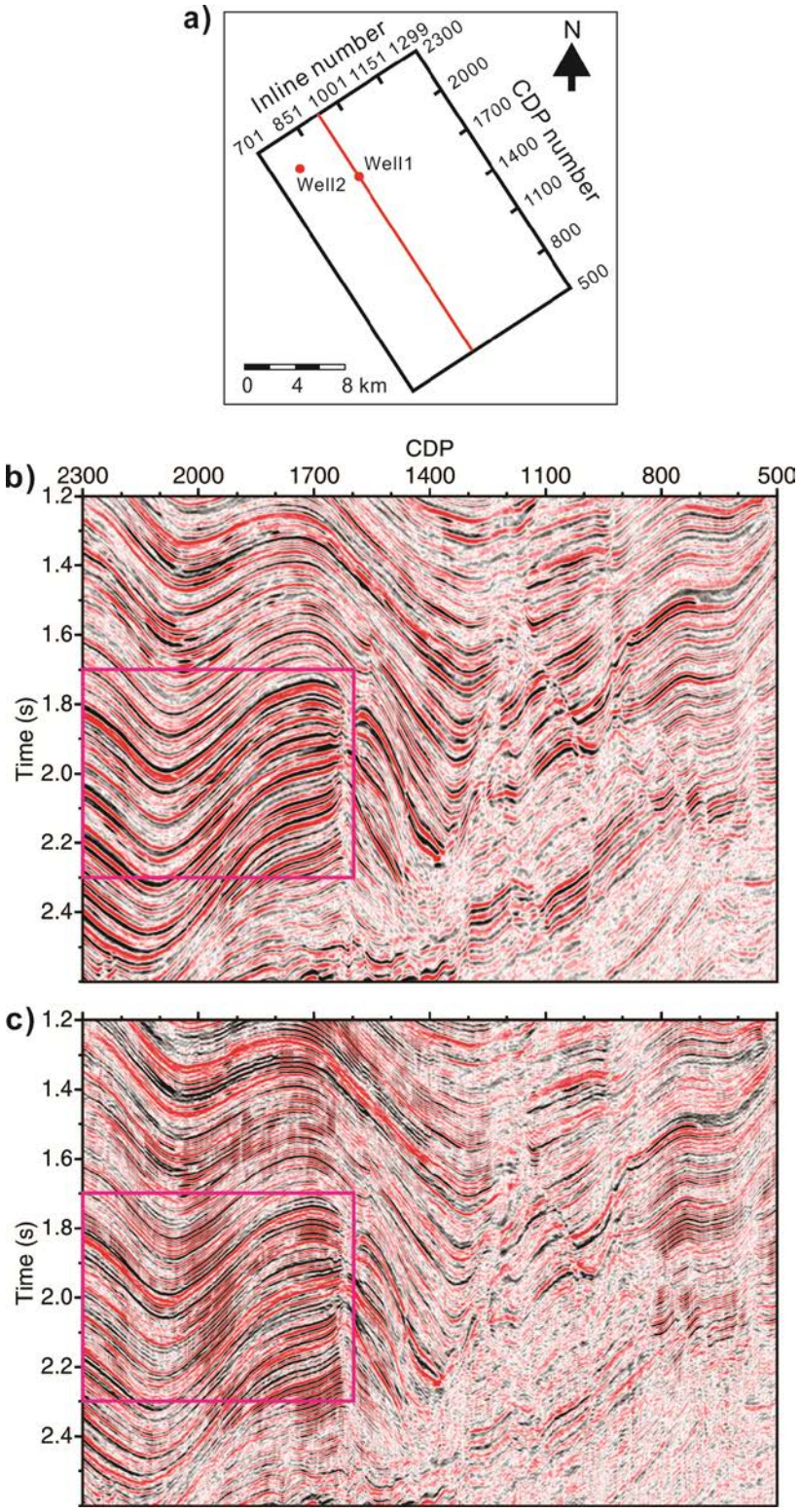

Figure 3. The 3D seismic data set. (*a*) The base map of the 3D seismic survey. The red line represents inline number 931 and the red dots indicate two well location. (*b*) Seismic profile (inline number 931, the red line in (*a*)), which presents seismic data within the CDP number between 500 and 2300 and the target time window between 1.2 and 2.6s. (*c*) The same seismic profile after the resolution enhancement.

EXTRACTING SEISMIC WAVELET

For extracting seismic wavelet, we assume that the reflectivity series is sufficiently random, and approximates the amplitude spectrum of the wavelet using the spectrum of the seismic data. Figure 4 displays the amplitude spectrum (in blue) of the seismic data. We evaluate the mean frequency by (Berkhout, 1984; Wang, 2015a)

$$f_m = \frac{\sum_f f\,|A(f)|^2}{\sum_f |A(f)|^2}, \tag{1}$$

where f is the frequency, and $|A(f)|$ is the Fourier magnitude (amplitude) spectrum. The mean frequency in Figure 4 is statistically evaluated to be 40.4 Hz. This mean frequency approximately equals to the central frequency, for generalized asymmetrical wavelets (Wang, 2015b).

We smooth the amplitude spectrum of the seismic data and use the resulting curve (in red, Figure 4) as the amplitude spectrum of the wavelet. We estimate a constant-phase angle from the seismic data based on kurtosis matching (White, 1988; Wang, 2016, Chapter 8). The black curve in Figure 5a is the wavelet extracted from seismic data, and the black curve in Figure 5b is its amplitude spectrum.

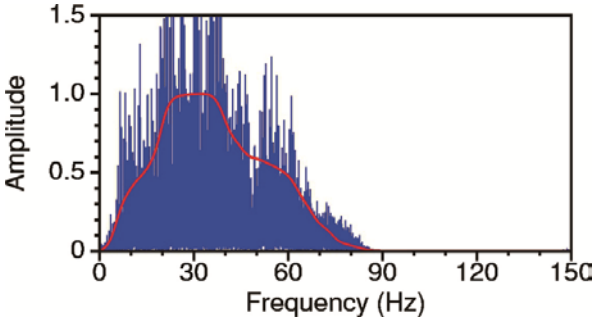

Figure 4. The Fourier magnitude (amplitude) spectra of the seismic data and the wavelet. The amplitude spectrum of the seismic data (blue), and the smoothed spectrum which is treated as the spectrum of the wavelet (red).

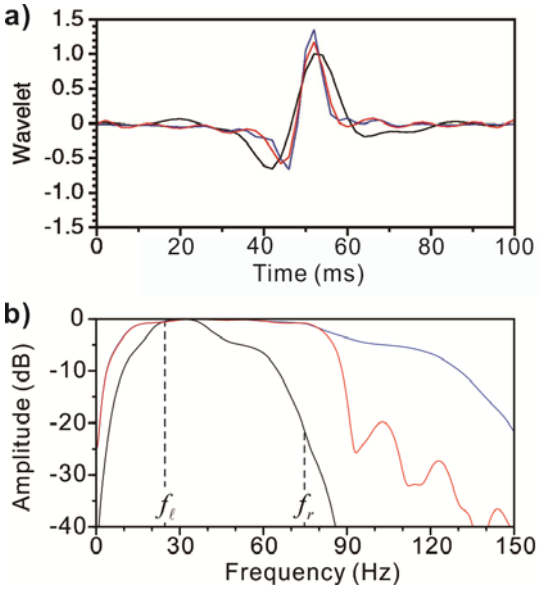

Figure 5. Wavelets and the amplitude spectra. (a) The extracted wavelet (black), the ideal band extended wavelet (blue), and the filtered wavelet (red). (b) Amplitude spectra of the extracted wavelet (black), the ideal band extended wavelet (blue), and the filtered wavelet (red).

We divide the 3D seismic data into different time windows from the shallow part to the deep part and extract a seismic wavelet from each window using the constant-phase wavelet estimation method. We find that the extracted wavelets are nearly the same for various time windows, because the 3D seismic data have been inverse-*Q* filtered and the amplitude attenuation of high-frequency components has been compensated. Therefore, in this study, we extract a single seismic wavelet for the entire 3D seismic cube.

CONSTRUCTING THE BAND EXTENSION FILTER

In this section, we construct the band extension filter, which stretches the frequency spectrum over the full frequency range. We call this band extension filter a full-band extension method. Note that the "band" here is the full frequency range and differs from the "bandwidth", which is measured at a half of the maximum amplitude level (Wang, 2015a, b).

We achieve the band extension by multiplying the frequency spectra of the original seismic wavelet with a frequency-dependent scaling factor $a(f)$,

$$a(f)=\begin{cases}\dfrac{f_\ell+3f}{4f_\ell}, & 0\le f<f_\ell,\\[2ex] \dfrac{f_r+f-2f_\ell}{f_r-f_\ell}, & f_\ell\le f<f_r,\\[2ex] 2, & f\ge f_r,\end{cases} \tag{2}$$

where f_ℓ and f_r are two reference frequencies (Figure 5a). The scaling factor varies between 0.25 and 1 for the frequency increases from 0 to the left reference f_ℓ, and between 1 and 2 for the frequency increases from the left reference f_ℓ to the right reference f_r.

Denote the frequency spectrum of a wavelet as $W(f)=|W(f)|e^{i\phi(f)}$, where $|W(f)|$ is the amplitude spectrum and $\phi(f)$ is the phase spectrum. When applying this frequency-dependent scaling factor $a(f)$ to the frequency spectrum, the entire spectrum will be stretched towards to both the low- and high-frequency axes, according to the following expression:

$$\hat{W}(f)=\frac{1}{\tilde{a}}\left|W\left(\frac{f}{a(f)}\right)\right|\exp\left(i\phi\left(\frac{f}{a(f)}\right)\right), \tag{3}$$

where $\hat{W}(f)$ is the frequency spectrum after the frequency domain stretching, and $\tilde{a}$ is the average of $a(f)$ over the frequency range between 0 Hz and the Nyquist value (250 Hz in the example shown in this paper).

From equations 2 and 3, we can see that when f decreases from the left reference frequency f_ℓ to 0, the spectrum is stretched towards the low-frequency direction. When f increases from the left reference frequency f_ℓ to the right reference frequency f_r, the spectrum is stretched towards the high-frequency direction. When $f\ge f_r$, the spectrum is simply shifted towards the high-frequency direction. Consequently the mean frequency f_m is shifted to a higher frequency.

The blue curves in Figure 5a-b are the compressed seismic wavelet and the stretched frequency spectrum, respectively. When the wavelet is compressed, the frequency band is extended and both the low frequency and high frequency components are stretched (Chen and Wang, 2018). The side lobes of the wavelet are compressed as well, and the form of the compressed wavelet becomes simpler. Therefore, we can easily identify the thin layer reflections.

For constructing the full-band extension filter, we use the following relationship between the originally estimated seismic wavelet $W(f)$ and the compressed seismic wavelet $\hat{W}(f)$:

$$W(f)H(f) = \hat{W}(f), \tag{4}$$

where $H(f)$ is the filter in the frequency domain. Under the least-squares sense, we can derive the filter as

$$H(f) = [\overline{W}(f)W(f) + \mu]^{-1}\overline{W}(f)\hat{W}(f), \tag{5}$$

where $\overline{W}(f)$ is the conjugate complex of $W(f)$, and μ is the stabilization factor. In this test, we set $\mu = 0.1\%$ of the maximum value of the power of the originally estimated wavelet. The stabilized filter $H(f)$ suppresses the ambient noise below this level, whereas it boosts the powers of both low- and high-frequencies.

Let us see the stabilization effect in Figure 5, in which the red curves are the amplitude spectrum (Figure 5b), after applying $H(f)$ to the spectrum of the estimated wavelet, and the corresponding wavelet (Figure 5a), respectively. It can be seen that, because of the stabilization factor, the actual filtered wavelet is somewhat different from the theoretically compressed wavelet. In application, stabilization and resolution must be balanced in field seismic data application.

Once we obtain the band extension filter $H(f)$, we apply it to the seismic data by frequency-domain multiplication:

$$\hat{D}(f) = H(f)D(f), \tag{6}$$

where $D(f)$ and $\hat{D}(f)$ are the frequency-domain seismic traces before and after band extension. Performing the inverse Fourier transform trace by trace produces the wavelet-compressed seismic data in the time domain.

APPLICATION TO FIELD SEISMIC DATA

The full-band extension workflow consists of four steps: estimating a seismic wavelet $w(t)$ from a field 3D seismic data set, stretching frequency spectrum from $W(f)$ to $\hat{W}(f)$ using frequency-dependent scaling factor $a(f)$, deriving a band extension filter $H(f)$, and applying the derived band extension filter $H(f)$ to the entire volume of the field 3D seismic data.

Figure 6 shows a zoomed-in version of the seismic profiles of inline number 931 (the red rectangular boxes shown in Figure 3b-c) before and after full-band extension. After the band extension filtering, seismic reflection events can be easily distinguished, which is helpful for the identification of rhythmites. In this zoomed-in version, reflection waveforms also present clear lateral variation along any reflection events.

Figure 7 compares the amplitude spectra of the seismic data profiles before and after full-band extension. Both the low frequencies and high frequencies have been stretched. The bandwidth does show significant change. Before the full-band extension, the bandwidth is between 7 and 70 Hz, while after the full-band extension, the bandwidth is between 2 and 90 Hz.

On the amplitude spectrum of Figure 7b, there is a persistent feature (amplitude gain) at about 70-90 Hz that appears as a horizontal zone across the data CDP's. It indicates that previous processes boosted the noise in frequencies higher than 70 Hz, and filtered the data using a taper defined within 70-90 Hz. The full-band extension process reveals this hidden problem by amplifying those filtered but noisy amplitudes which were less than –20 dB within the tapering range.

Although we compared the amplitude spectra here, the full-band extension filter alters both the amplitude and phase spectra. This differs from a conventional spectral whitening technique operating only on the amplitude spectrum of a seismic trace. Since the spectral whitening technique is a pulse-compression method without concern for the phase of the wavelet, the results can be

misleading when performing stratigraphic interpretation unless the input wavelet is zero-phase wavelet.

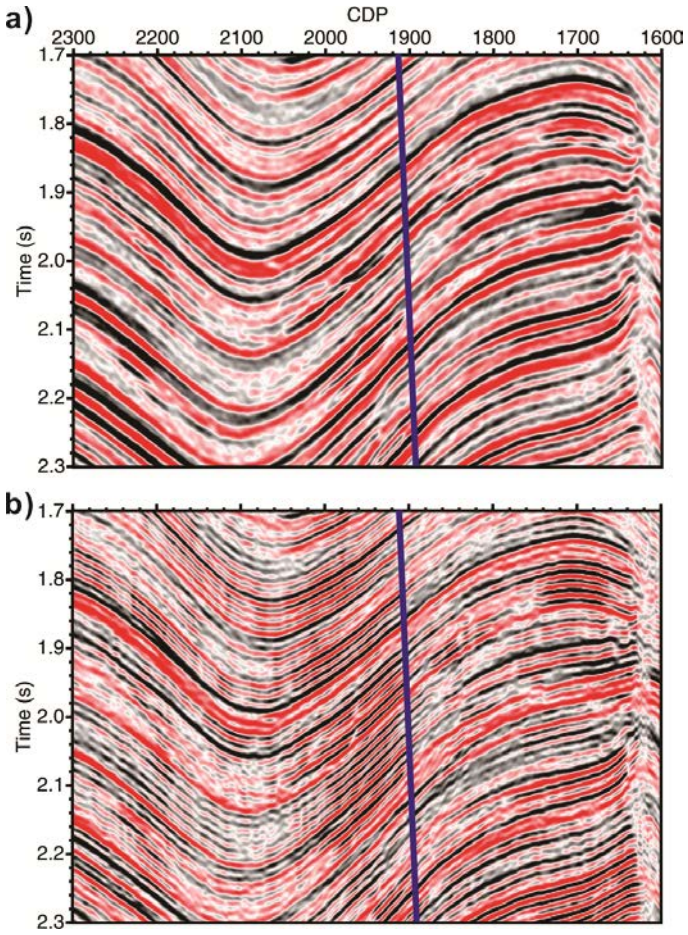

Figure 6. Seismic resolution enhancement. (a) Zoomed-in version of the seismic profile before the full-band extension. (b) Zoomed-in version of the seismic profile after the full-band extension. The blue line indicates a well drilling path.

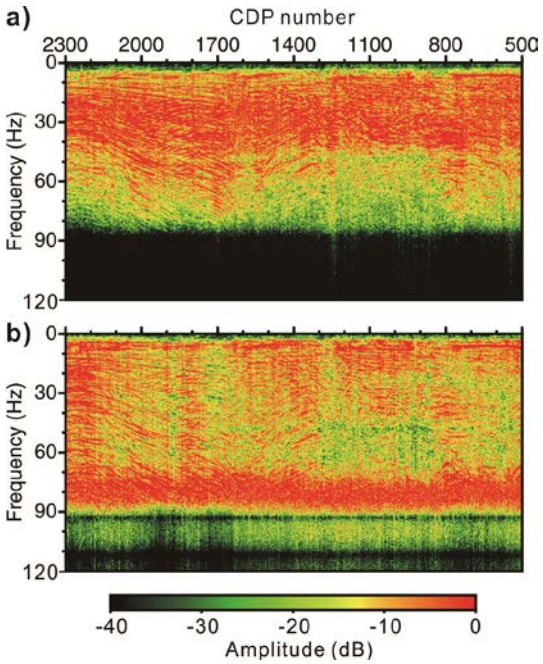

Figure 7. Seismic resolution enhancement. (a) Frequency spectra of a seismic profile before the full-band extension. (b) Frequency spectra of the seismic profile after the full-band extension.

We can see from Figure 8a that, after the full-band extension, additional reflection events appear along the well path. In the gamma ray curve (at Well 1), high gamma values indicate salt rhythmites. The arrow-pointed events in the processed seismic data are obviously consistent with the gamma ray curves. We can also see from Figure 8b that those added events in the seismic data after the full-band extension correspond to the stratigraphic layers, such as stratigraphic layers Q_3^{1b} and Q_3^3, Q_4^0. Those reflections are not visible in the profile before the full-band extension.

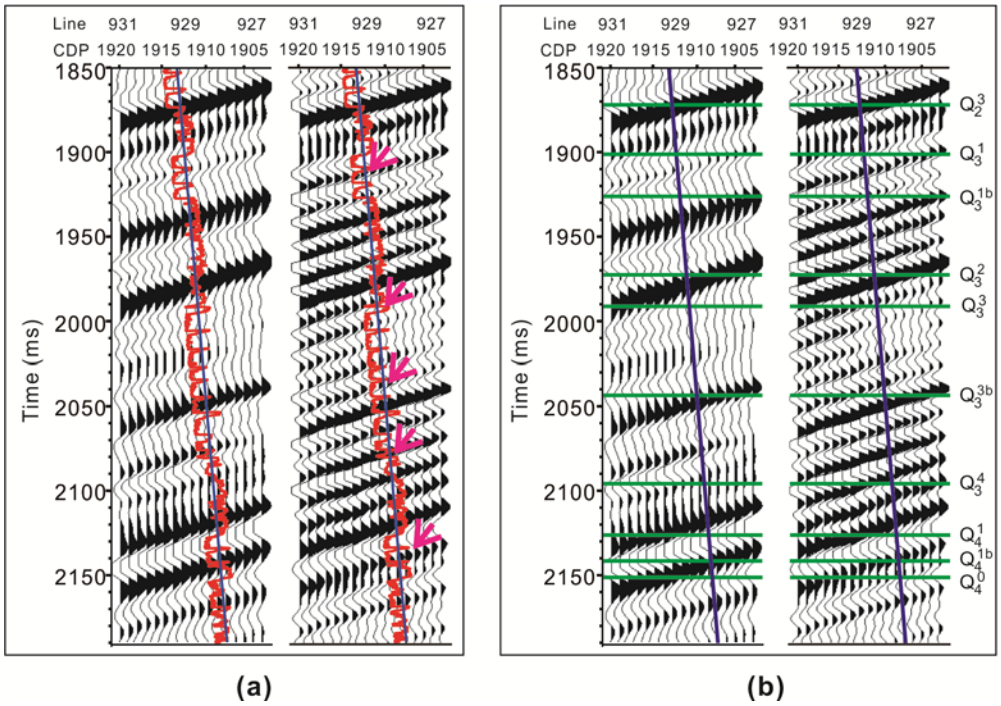

Figure 8. (a) Comparison with the Gamma ray curve at Well 1 (Figure 6a). (b) Sequential stratigraphic interpretation. The left and right panels in each figure represent the seismic data before and after the full-band extension. Numbers in blue and black at the top of each figure are inline and crossline numbers, respectively.

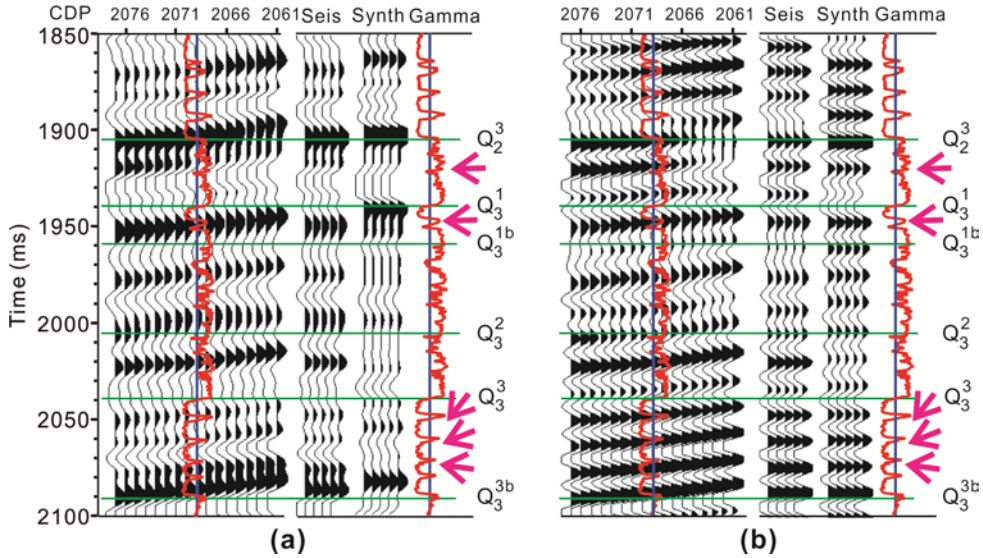

Figure 9. (a) Comparison of the Gamma ray (at Well 2 of Figure 3a) with the seismic data before band extension, the seismic trace (re-plotted 5 times), the synthetic trace (re-plotted 5 times) at the well location, and the Gamma ray curve for stratigraphic interpretation. (b) Comparison of the Gamma ray curve with the seismic data after the full-band extension, the re-plotted seismic trace, the re-plotted synthetic trace at the well location, and the Gamma ray curve for stratigraphic interpretation.

Figure 9 shows another comparison between seismic data and the Gamma ray curve of a vertical well (Well 2, at CDP 2069 of inline number 781). In Figure 9a-b, we compare the gamma ray with the seismic data before and after the full-band extension. In addition, in each case, we compare both the field and synthetic seismic traces (at well location) with the gamma ray. Extra events (indicated by arrows between marked stratigraphic interfaces) in the band extended seismic trace are also verified by the synthetic trace.

Figure 10 compares time slices (at time 2 s) of seismic data (a) and the instantaneous phases (b), before and after band extension. The comparison indicates that the spatial resolution of the 3D seismic data has been improved significantly by the full-band extension.

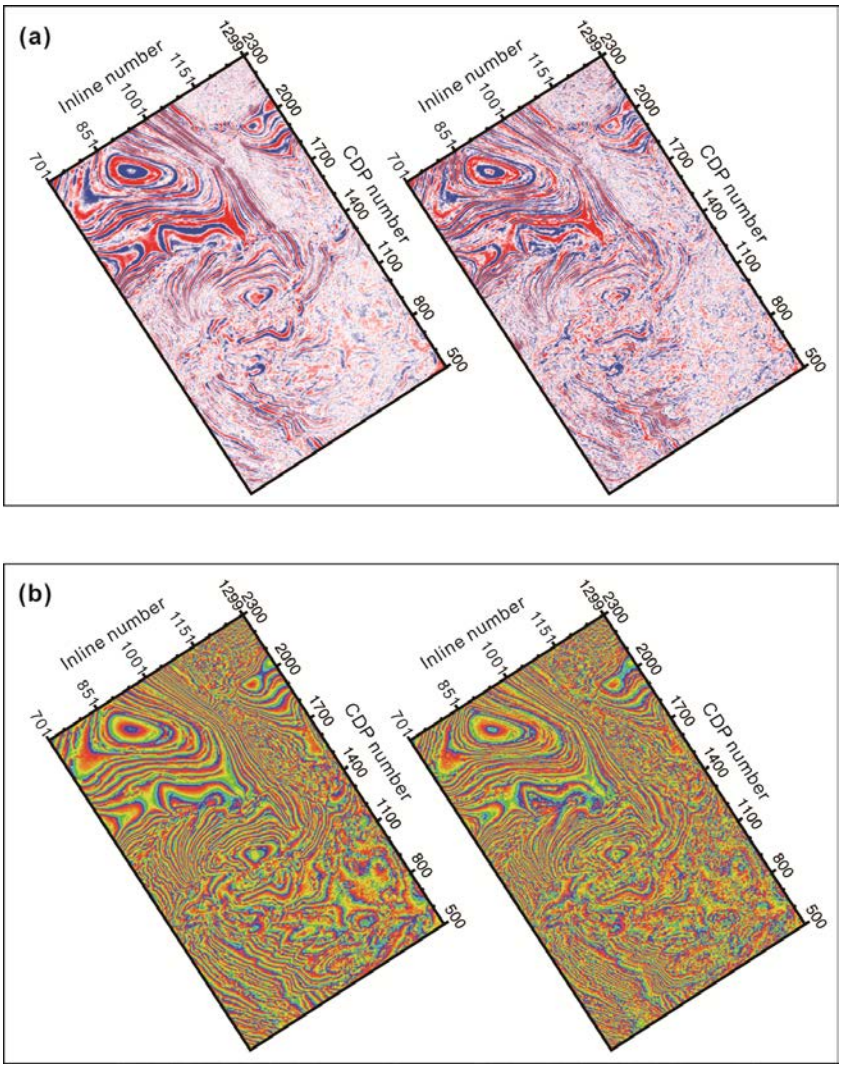

Figure 10. (a) Time slices of seismic data before and after band extension. (b) Time slices of the instantaneous phases before and after band extension. The spatial resolution has been improved significantly by the full-band extension.

Note that we constructed the full-band extension filter in the least-squares sense (equation 5). In order to construct the filter with a gentle slope, we should preserve the high-frequency components of seismic data during pre-processing. In this paper, we used a single seismic wavelet for the entire data set. However, if the seismic data have not been compensated for the attenuation effect with inverse Q filtering during pre-processing, we would need to estimate a series of wavelets for different time windows, and to implement full-band extension in a time-varying fashion.

CONCLUSIONS

We have presented the full-band extension method for the enhancement of 3D seismic resolution. We have implemented the method in three steps, wavelet extraction, filter construction and data filtering. We have improved both the vertical resolution and the lateral resolution of 3D seismic data. This work would be helpful for the identification of rhythmites in the Q Depression, and furthermore the shale-oil detection.

ACKNOWLEDGMENTS

The authors are grateful to the National Natural Science Foundation of China (grant nos. U1663207, 41622405 and 41704136), National Basic Research Program (973 Program, grant no. 2014CB239104), the Major National Science and Technology Projects of China (grant no. 2017ZX05049-002), China Postdoctoral Science Foundation (grant no. 2016M601080), and the Science Foundation of China University of Petroleum (Beijing) (grant no. 2462018BJC001), for supporting this research.

REFERENCES

Berkhout, A. J., 1984, Seismic Resolution – Resolving Power of Acoustical Echo Techniques: Geophysical Press.

Chen, S. Q., and Y. Wang, 2018, Seismic resolution enhancement by frequency-dependent wavelet scaling: IEEE Geoscience and Remote Sensing Letters, **15**, 654–658, doi: 10.1109/LGRS.2018.2809564.

Chen, Z., Y. Wang, X. Chen, and J. Li, 2013, High-resolution seismic processing by Gabor deconvolution: Journal of Geophysics and Engineering, **10** (6), article number 065002, doi: 10.1088/1742-2132/10/6/065002.

Fang, Z., 2002, Hydrocarbon exploration signification of intersalt sediments in Qianjiang Saline Lake Basin: Acta Sedimentologica Sinica, **20**, 608–613, doi: 10.3969/j.issn.1000-0550.2002.04.012 (in Chinese).

Gan, Q., D. Xu, J. Tang, and, Y. Wang, 2009, Seismic resolution enhancement for tight-sand gas reservoir characterization: Journal of Geophysics and Engineering, **6**, 21–28, doi: 1088/1742-2132/6/1/002.

Guo, J., and Y. Wang, 2004, Recovery of a target reflection underneath coal seams: Journal of Geophysics and Engineering, **1**, 46–50, doi: 10.1088/1742-2132/1/1/005.

Hou, Y., F. Wang, S. He, T. Dong, and S. Wu, 2017, The properties and shale-oil potential of saline lacustrine shales in the Qianjiang Depression, Jianghan Basin, China: Marine and Petroleum Geology, **86**, 1173–1190, doi: 10.1016/j.marpetgeo.2017.07.008.

Huang, C., K. Chen, and X. Yang, 2002, Characteristics of sequence stratigraphy in the Saline Lake Basin: Journal of Oil & Gas Geology, **23** (2), 134–138, doi: 10.11743/ogg20020206.

Margrave, G. F., P. C. Gibson, J. P. Grossman, D. C. Henley, V. Iliescu, and M. P. Lamoureux, 2005, The Gabor transform, pseudo differential operators, and seismic deconvolution: Integrated Computer-Aided Engineering, **12**, 43–55.

Margrave, G. F., M. P. Lamoureux, and D. C. Henley, 2011, Gabor deconvolution: Estimating reflectivity by nonstationary deconvolution of seismic data: Geophysics, **76** (3), W15–W30, doi:

10.1190/1.3560167.

Robinson, E. A., 1967, Predictive decomposition of time series with application to seismic exploration: Geophysics, **32**, 418–484, doi: 10.1190/1.1439873.

Robinson, E. A., and S. Treitel, 1967, Principles of digital Wiener filtering: Geophysical Prospecting, **15**, 311–332, doi: 10.1111/j.1365-2478.1967. tb01793.x.

Peacock, K. L., and S. Treitel, 1969, Predictive deconvolution – Theory and practice: Geophysics, **34**, 155–169, doi: 10.1190/1.1440003.

Wang, Y., 2002, A stable and efficient approach of inverse *Q* filtering: Geophysics, **67**, 657–663, doi: 10.1190/1.1468627.

Wang, Y., 2006, Inverse *Q*-filter for seismic resolution enhancement: Geophysics, **71** (3), V51–V60, doi: 10.1190/1.2192912.

Wang, Y., 2008, Seismic Inverse *Q* Filtering: Blackwell, Oxford.

Wang, Y., 2015a, Frequencies of the Ricker wavelet: Geophysics, **80** (2), A31–A37, doi: 10.1190/GEO2014-0441.1

Wang, Y., 2015b, Generalized seismic wavelets: Geophysical Journal International, **203**, 1172–1178, doi: 10.1093/gji/ggv346.

Wang, Y., 2016, Seismic Inversion, Theory and Applications: Wiley Blackwell.

White, R. E., 1988, Maximum kurtosis phase correction: Geophysical Journal International, **95**, 371–389.

Zhao, S., and Y. Wang, 2004, Relative amplitude preserved P-P and P-SV wave seismic sections: Journal of Geophysics and Engineering, **1**, 259–262, doi: 10.1088/1742-2132/1/4/003.

Zheng, Y., 2010, Exploration direction and strategy for lithological accumulations in Qianjiang Formation of the Qianjing Sag, Jianhan Basin: Petroleum Geology and Experiment, **32**, 330–332 (in Chinese).

Zhou B. Z., I. M Mason, and P. J. Hatherly, 2007, Tuning seismic resolution by heterodyning: Journal of Geophysics and Engineering, **4**, 214–223, doi:10.1088/1742-2132/4/2/010.